


Oxidation of Metals
<https://doi.org/10.1007/s11085-021-10046-7>

ORIGINAL PAPER



The Effect of Al on the Formation of a CrTaO₄ Layer in Refractory High Entropy Alloys Ta-Mo-Cr-Ti-xAl

S. Schellert¹  · B. Gorr² · H.-J. Christ¹ · C. Pritzel³ · S. Laube² · A. Kauffmann² · M. Heilmaier²Received: 28 May 2021 / Revised: 28 May 2021 / Accepted: 31 May 2021
© The Author(s) 2021

Abstract

In this study, the effect of Al on the high temperature oxidation of Al-containing refractory high entropy alloys (RHEAs) Ta-Mo-Cr-Ti-xAl ($x=5; 10; 15; 20$ at%) was examined. Oxidation experiments were performed in air for 24 h at 1200 °C. The oxidation kinetics of the alloy with 5 at% Al is notably affected by the formation of gaseous MoO₃ and CrO₃, while continuous mass gain was detected for alloys with the higher Al concentrations. The alloys with 15 and 20 at% Al form relatively thin oxide scales and a zone of internal corrosion due to the formation of dense CrTaO₄ scales at the interface oxide/substrate. The alloys with 5 and 10 at% Al exhibit, on the contrary, thick and porous oxide scales because of fast growing Ta₂O₅. The positive influence of Al on the formation of Cr₂O₃ followed by the growth of CrTaO₄ to yield a compact scale is explained by getter and nucleation effects.

Keywords Refractory high entropy alloy · Al effect · CrTaO₄ formation · Getter effect

Introduction

The search for new materials that exceed the high temperature capabilities of modern Ni-based superalloys has endured for many decades. In line with the recently introduced concept of high entropy alloys [1], Senkov et al. [2] suggest RHEA as promising candidates for demanding high temperatures applications. Some RHEAs indeed possess outstanding mechanical properties above 1200 °C [3, 4] on which most studies were focused in the past. Much less attention has been paid to oxidation resistance of RHEA [5–9] though this feature is commonly known as one of the major drawbacks of refractory metals and refractory metal-based alloys. Recently, several RHEAs were

✉ S. Schellert
steven.schellert@uni-siegen.de

Extended author information available on the last page of the article

reported to possess a relatively high level of oxidation resistance due to the formation of compact CrTaO_4 scales [6–8, 10]. The rutile-type CrTaO_4 oxide forms by the reaction $\text{Cr}_2\text{O}_3 + \text{Ta}_2\text{O}_5 \rightarrow 2\text{CrTaO}_4$ [11, 12], which is decisive in terms of the oxidation resistance. In our recent studies, the oxidation behavior of the equiatomic RHEA Ta–Mo–Cr–Ti–Al, which is a CrTaO_4 -former, has been extensively investigated and the oxidation mechanism identified [8, 13]. In the temperature range 900–1100 °C, this alloy forms a complex oxide layer consisting of TiO_2 , Al_2O_3 , Cr_2O_3 and CrTaO_4 . The high oxidation resistance is, however, attributed to the formation of a continuous CrTaO_4 layer at the interface oxide/substrate as Al_2O_3 and Cr_2O_3 do not grow to fully compact scales. Up to date, no comprehensive study on the Al effect on the formation of such complex scales as CrTaO_4 exists in literature. Li et al. reported that the removal of Al from the alloy system Ta–Mo–Cr–Ti–Al leads to a superior oxidation resistance at 1000 °C for 10 h due to the formation of a continuous CrTaO_4 layer [10]. However, the reason for such improved oxidation behavior of the TaMoCrTi alloy was not provided. In this work, the effect of Al on the oxidation resistance of the Al-containing alloys Ta–Mo–Cr–Ti–xAl ($x=5; 10; 15; 20$ at%) at 1200 °C is systematically investigated. Thereby, the key question of how Al influences the formation of a compact CrTaO_4 layer will be clarified.

Experimental Procedures

The details about the manufacturing process and the sample preparation procedure can be found elsewhere [8]. All alloys were homogenized in a tube furnace at 1500 °C for 20 h under Ar. Isothermal oxidation tests were performed in a thermogravimetric system at 1200 °C for 24 h. In addition, all alloys were oxidized for 30 min to study the transient oxidation. To identify the oxidation products, various methods were used. The identification of crystalline phases was performed in a X-ray diffractometer X'Pert Pro MPD with Cu-K α radiation operating at 45 kV and 40 mA. To characterize the microstructure of the alloys and the oxide scales, a focused ion beam–scanning electron microscope (FIB–SEM) DualBeam system of type FEI Helios Nanolab 600 equipped with techniques such as backscatter electron (BSE) imaging, energy-dispersive X-ray spectroscopy (EDX) was used. The oxide layer thicknesses and the element distribution in oxide scales were determined on the basis of BSE images and EDX mappings. For this purpose, 20 measurements were performed using the software ImageJ. The outer oxide scale of the alloy Ta–Mo–Cr–Ti–5Al for the TEM investigations was removed using a scalpel and placed on a TEM grid. The following TEM investigations were performed in TEM FEI Talos F200X with 200 kV acceleration voltage.

Results

To understand the Al effect in detail, the microstructure of a series of alloys within the system Ta–Mo–Cr–Ti–xAl ($x=5; 10; 15; 20$ at%) was investigated. Comprehensive information on the microstructure of the equiatomic Ta–Mo–Cr–Ti–20Al has already been reported in Ref. [8, 14]. After homogenization, this alloy consists of

large grains of the ordered B2 crystal structure as well as some Laves phase predominantly decorating the grain boundaries. The results of microstructural investigations performed on Ta-Mo-Cr-Ti-5Al are displayed in Fig. 1. XRD analysis depicted in Fig. 1a reveals peaks that can be attributed to an A2-type crystal structure (W prototype, closed circles). Furthermore, weak occurrence of the {100} superlattice peak of the B2 superstructure of A2 is observed (CsCl prototype, open circles). In addition, the C14-type Laves phase Cr_2Ta (MgZn_2 -type, hatched squares) is detected. BSE images illustrated in Fig. 1b. and c. reveal that only grain boundaries are decorated with the Laves phase (bright contrast). This microstructure is representative also for alloys with the higher Al concentrations of 10 and 15 at%. Thus, the microstructure of these alloys is not shown here. It should, however, be mentioned that all alloys are not in the thermodynamic equilibrium after heat treatment; therefore, it is expected that the amount of the Laves phase increases during oxidation [14].

The kinetic oxidation curves of the alloys Ta-Mo-Cr-Ti-xAl ($x=5; 10; 15; 20$ at%) recorded during isothermal exposure to air at 1200 °C for 24 h are shown in Fig. 2. The initial kinetics of the alloy Ta-Mo-Cr-Ti-5Al is extremely rapid. But after about 7 h, the value of the mass change did not change notably during approximately 10 h; afterward, however, a linear mass gain was recorded. Overall, the alloy Ta-Mo-Cr-Ti-5Al reveals the highest mass gain value after 24 h of exposure. In contrast, the alloy Ta-Mo-Cr-Ti-10Al shows significantly lower initial kinetics followed by a continuous linear mass gain after approximately 15 h. This alloy yields the lowest mass gain after 24 h exposure. The kinetic curves of the alloys with the higher Al contents (15 and 20 at%) obey the nearly parabolic rate law.

In order to explore the nature of corrosion products, XRD analysis was performed on samples oxidized for 24 h at 1200 °C. XRD measurements were also conducted on samples which were exposed to air in a furnace for 30 min at 1200 °C. Figure 3a shows exemplify diffractogram of the alloy Ta-Mo-Cr-Ti-5Al after oxidation for 24 h at 1200 °C. All results of X-ray diffraction analyses conducted on alloys Ta-Mo-Cr-Ti-xAl ($x=5; 10; 15; 20$ at%) after oxidation for 30 min and 24 h at 1200 °C are summarized in Table 1. The diffractogram includes Al_2O_3 , Cr_2O_3 , TiO_2 , Ta_2O_5 and CrTaO_4 . Independent on the test time and the Al content, Al_2O_3 , TiO_2 and Cr_2O_3 were identified on all alloys. The only difference was noted for the appearance of T_2O_5 and CrTaO_4 . In the alloy Ta-Mo-Cr-Ti-5Al, both Ta_2O_5 and

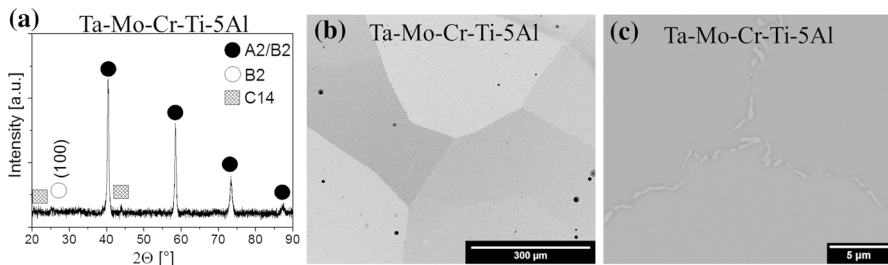


Fig. 1 Microstructure of the alloy Ta-Mo-Cr-Ti-5Al after heat treatment at 1500 °C for 20 h: **a.** Powder XRD pattern, **b.** and **c.** BSE micrographs with overview and grain boundary detail

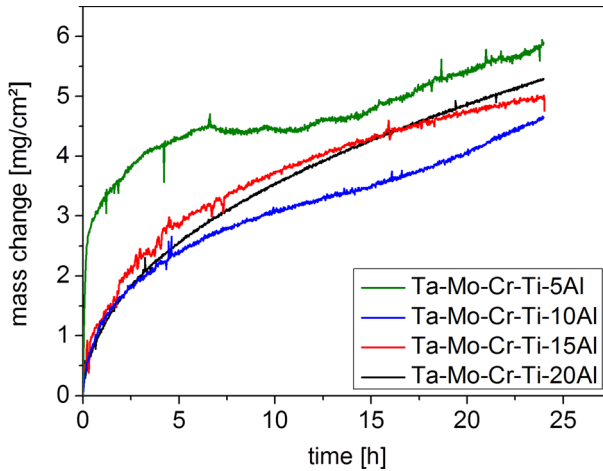


Fig. 2 Specific mass change as a function of time for Ta-Mo-Cr-Ti-xAl ($x=5; 10; 15; 20$ at%) during isothermal exposure to air at $1200\text{ }^{\circ}\text{C}$ for 24 h

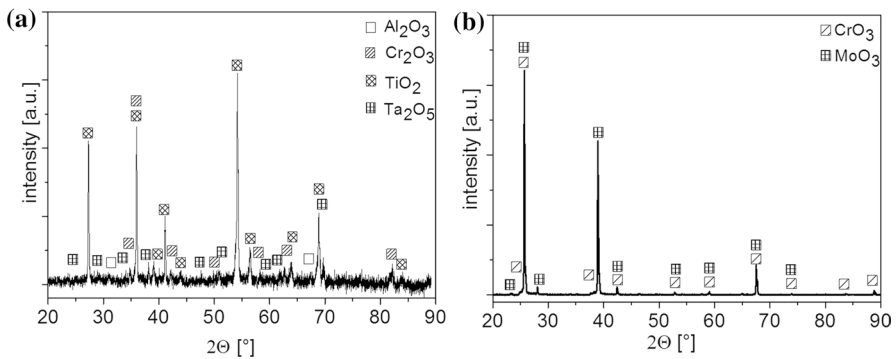


Fig. 3 Results of XRD analysis of **a.** Ta-Mo-Cr-Ti-5Al after 24 h oxidation in air at $1200\text{ }^{\circ}\text{C}$ and **b.** substances scraped off the platinum wire after 24 h oxidation of the alloy Ta-Mo-Cr-Ti-5Al

CrTaO_4 were detected after 30 min oxidation. However, only Ta_2O_5 was identified after 24 h oxidation. In case of the alloy Ta-Mo-Cr-Ti-10Al, on the contrary, only CrTaO_4 could be detected after 30 min exposure to air, while both oxides were observed after 24 h oxidation. In Ta-Mo-Cr-Ti-15Al and the equiatomic RHEA with 20 at% Al, only CrTaO_4 was found after both exposure times. Further, after 24 h oxidation of all alloys, a yellow substance was detected on the platinum wire of the thermogravimetric system. The amount of this substance decreases with increasing Al content. However, the influence by re-deposited substances on the sample and the Pt sample carrier is neglected. The re-deposition on samples can only take place during cooling, i.e., when the continuous recording of the mass change was stopped. The substances were carefully scraped off and examined by X-ray spectroscopy which revealed that MoO_3 evaporated from all alloys and condensed on parts of the

Table 1 XRD results of Ta-Mo-Cr-Ti-xAl ($x=5; 10; 15; 20$ at%) after 30 min and 24 h oxidation at 1200 °C in air (“X” indicates that the corresponding oxide was detected)

Alloy	Ta-Mo-Cr-Ti-5Al		Ta-Mo-Cr-Ti-10Al		Ta-Mo-Cr-Ti-15Al		Ta-Mo-Cr-Ti-20Al	
	30 min	24 h	30 min	24 h	30 min	24 h	30 min	24 h
Al ₂ O ₃ (corundum)	X	X	X	X	X	X	X	X
Cr ₂ O ₃ (corundum)	X	X	X	X	X	X	X	X
TiO ₂ (rutile)	X	X	X	X	X	X	X	X
Ta ₂ O ₅ (orthohombic)	X	X		X				
CrTaO ₄ (rutile)	X		X	X	X	X	X	X

thermogravimetric system. Additionally, the XRD analysis indicates the presence of CrO₃ in case of the alloys Ta-Mo-Cr-Ti-5Al and Ta-Mo-Cr-Ti-10Al. Figure 3b. gives an example of the diffractogram of the substances collected after 24 h oxidation of the alloy Ta-Mo-Cr-Ti-5Al.

Cross-sectional images of the oxide layers after 30 min and 24 h of oxidation in air are depicted in Fig. 4. All oxide scales generally show a complex multi-layered structure. The common feature of the oxide layers formed on all alloys is the outer oxide scale which consists of a mixture of Al₂O₃, TiO₂ and Cr₂O₃ particles as well as a semi-continuous Cr₂O₃ scale underneath. Below this outer oxide layer, the oxide scales differ significantly depending on the Al content and oxidation time. In the following, this oxide layer will be designated as inner oxide scale. The inner oxide scale of the alloy Ta-Mo-Cr-Ti-5Al has a heterogeneous character after 30 min oxidation. Regions of a thin, continuous CrTaO₄ layer but also thicker scales consisting of Al₂O₃, TiO₂ and Cr₂O₃ in addition to the major phase Ta₂O₅ were observed. After 24 h of oxidation, the thicknesses of the oxide layers vary strongly, whereby the scales consist of mixed Ti, Ta, Cr oxides (see Fig. 4a). Spalling of the oxide scale was observed only in Ta-Mo-Cr-Ti-5Al after oxidation for 24 h. The delamination of the oxide scale occurs during the cooling process since no sudden mass change during the oxidation was detected. By contrast, the alloy Ta-Mo-Cr-Ti-10Al reveals the formation of an inner oxide scale consisting of CrTaO₄ during the initial oxidation. However, after 24 h of exposure, thick scales predominantly containing Ta₂O₅ were identified in addition to the thin CrTaO₄ scales (see Fig. 4b.). In contrast, the alloys Ta-Mo-Cr-Ti-15Al and Ta-Mo-Cr-Ti-20Al reveal an inner CrTaO₄-based oxide scale which was identified after first 30 min of oxidation and which remains intact at least up to 24 h of exposure (see Fig. 4c. and d.). Below the inner oxide scale, a pronounced internal oxidation was observed which manifests itself in the formation of Al₂O₃ and TiN particles. Generally, TiN precipitates deeper in comparison to Al₂O₃ particles.

In order to describe the Al effect on the formation of the oxide scales and their growth quantitatively, the thicknesses of (i) the total oxide scale, (ii) the outer oxide layer consisting of Al₂O₃, Cr₂O₃, TiO₂ particles and a discontinuous Cr₂O₃, scale, (iii) the total zone of internal corrosion and (iv) the zone of internal corrosion with Al₂O₃ particles were determined after 30 min and 24 h oxidation at 1200 °C (see

Fig. 5). It is clear that the depth of the total zone of internal corrosion ($\text{TiN} + \text{Al}_2\text{O}_3$) increases with oxidation time and generally decreases with increasing Al concentration. Though, the depth of the Al_2O_3 particles in the zone of internal corrosion becomes progressively enhanced with increasing Al content after both oxidation times. The more pronounced zone of internal corrosion in the alloy Ta-Mo-Cr-Ti-20Al can be explained by the considerably coarser TiN particles compared to those formed in the alloy with 15 at% Al (see Fig. 4). The entire oxide layers become progressively thicker with decreasing Al content and longer oxidation time. Interestingly, the thicknesses of the outer oxide scales formed after 30 min oxidation increase with the Al concentrations. This dependence vanishes, however, nearly completely after 24 h oxidation. The equimolar alloy exhibits the thinnest oxide scale, while the most dramatic oxidation attack was detected for the alloy with the lowest Al concentration. The large error bars determined for the alloys with 5 and 10 at% Al reflect the severe inhomogeneity observed in the oxide layer thickness. In contrast to the alloys with the low Al concentrations, the oxide scales formed on the alloys with 15 and 20 at% Al are more homogeneous, and the scale thickness difference between these alloys is marginal.

In order to better understand the constitution of the initially formed oxide scales as well as those formed during steady-state period of oxidation, the element distribution in the outer oxide scale was analyzed using SEM–EDX mappings. To determine the element distribution, EDX mappings representing the elements via color contrast were evaluated. In addition, the EDX data were correlated with the BSE images, allowing to conclude the chemical contrast via the resulting grayscale variation. This approach allows to obtain a holistic result.

Results shown in Fig. 6a clearly reveal that the concentrations of Al and Cr in the outer layer formed after 30 min oxidation enhance with the increasing Al content. This implies that a higher amount of Al_2O_3 and Cr_2O_3 is present in the alloys with the higher Al concentrations. It should, however, be mentioned that the outer oxide layer mainly consists of TiO_2 (see Fig. 6a).

While the thickness of the outer oxide layer does not change notably with the Al concentration during exposure for 24 h (see Fig. 5b), the constitution of the outer

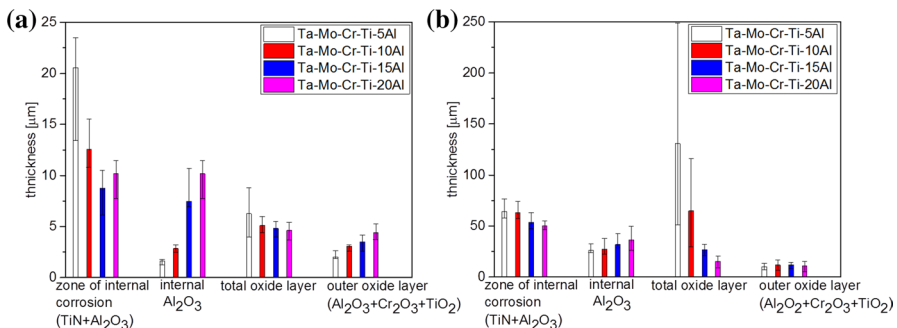


Fig. 5 Thickness of the total zone of internal corrosion ($\text{TiN} + \text{Al}_2\text{O}_3$), the zone of internal corrosion with Al_2O_3 particles only, the total oxide layer and the outer oxide layer ($\text{Al}_2\text{O}_3 + \text{Cr}_2\text{O}_3 + \text{TiO}_2$) after **a.** 30 min oxidation at 1200 °C and **b.** 24 h oxidation at 1200 °C

oxide layer changes substantially. With the increasing Al concentration, notably more Cr and less Ti were found in the outer oxide layer. As mentioned previously, Cr was found as condensed CrO_3 on different parts of the thermogravimetric device during oxidation Ta-Mo-Cr-Ti-5Al and Ta-Mo-Cr-Ti-10Al indicating evaporation of CrO_3 . Furthermore, it is interesting to note that the alloy Ta-Mo-Cr-Ti-10Al forms large Al_2O_3 particles, while fine particles were found in the outer scale formed on the alloy Ta-Mo-Cr-Ti-15Al. In case of the equiatomic alloy, Al_2O_3 and Cr_2O_3 particles were found near each other or even at the same location presumably indicating a solid solution.

To verify the results obtained using SEM–EDX and presented in Fig. 6, additional TEM investigations were carried out on the alloy Ta-Mo-Cr-Ti-5Al oxidized for 30 min at 1200 °C. The outer oxide layer was placed on a TEM grid (see Fig. 7a and b). TEM–EDX analyses were performed on different locations. The determined volume fractions of Al, Cr and Ti confirm the corresponding values of the element distribution found using SEM–EDX (compare Fig. 7c and Table 2 with Fig. 6a).

Discussion

The results presented above reveal a clear tendency that the oxidation resistance enhances with increasing Al content in the alloy system Ta-Mo-Cr-Ti-xAl, although no dense and continuous Al_2O_3 scale was formed. Instead, CrTaO_4 scales, which ensure a reasonable level of oxidation resistance, were identified in alloys possessing Al concentrations higher than 10 at%. Only two earlier studies were found describing the oxidation behavior of alloys with a similar chemical composition. The oxidation results of 25.2Cr-17.6Al-20.3Mo-15.2Nb-2.9Si-13.4Ta-5.4Ti [at%] proposed by Lo et al. [6] are in agreement with those presented in our study. In this RHEA, which contains 17.6 at% Al, a continuous CrTaO_4 layer was observed after 200 h oxidation at 1100 °C. A completely opposite conclusion was drawn by Li et al. in terms of the Al effect in RHEA [10]. Though both alloys, Al-free MoTaTiCr and Al-containing MoTaTiCrAl, are CrTaO_4 -formers, the Al-free alloy exhibits a better oxidation behavior after oxidation for 10 h at 1000 °C as compared to the Al-containing

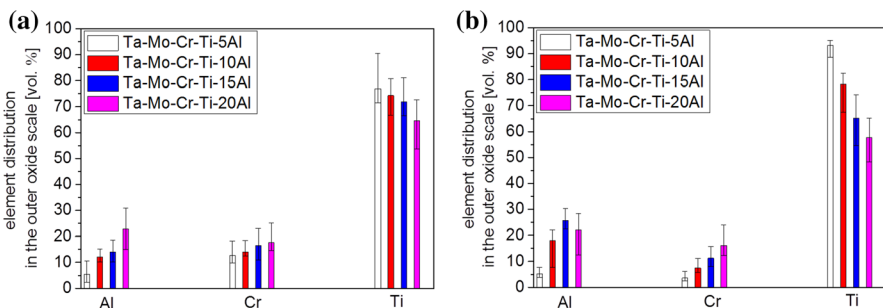


Fig. 6 Distribution of Al, Cr and Ti in the outer oxide layer after **a.** 30 min oxidation at 1200 °C and **b.** 24 h oxidation at 1200 °C

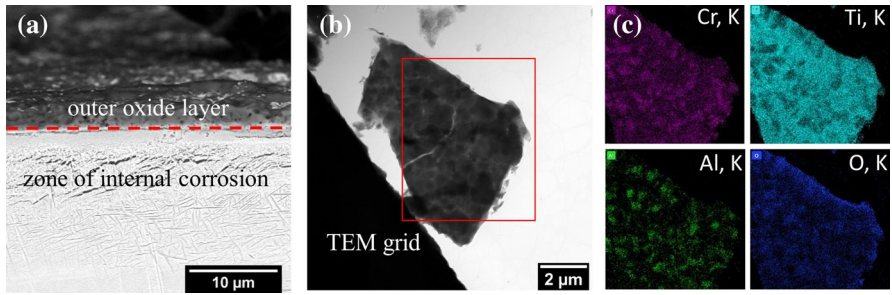


Fig. 7 Investigation of the elemental distribution in the outer layer **a.** BSE image of the alloy Ta-Mo-Cr-Ti-5Al after oxidation for 30 min (upper oxide layer was removed and analyzed in TEM) **b.** STEM-HAADF image of the removed outer oxide layer **c.** corresponding EDX mapping of the image marked as a red area in **(b)** (Color figure online)

Table 2 Element distribution in the outer oxide layer of the alloy Ta-Mo-Cr-Ti-5Al after oxidation for 30 min using TEM-EDX

Element	Al	Cr	Ti
Element distribution [vol. %]	4^{+5}_{-2}	14^{+6}_{-5}	76^{+9}_{-5}

one. Unfortunately, the reason for such superior oxidation resistance of the alloy MoTaTiCr was not given in [10].

The results of oxidation kinetics and microstructural investigation of oxide scales formed on alloys studied in this work can be explained by the corrosion products formed during oxidation. The rapid mass gain during initial oxidation of the alloy Ta-Mo-Cr-Ti-5Al (see Fig. 2) can be attributed to the formation of the fast growing Ta_2O_5 (see Fig. 4a) [15]. Furthermore, due to its unfavorable PBR ratio of 2.5, the detrimental formation of Ta_2O_5 obviously results in buckling of the oxide layer which propagates with time facilitating the inward transport of oxygen and nitrogen [16]. It can further be assumed that the nitrogen inward diffusion in this alloy substantially contributes to the high values of the mass gain as the thickest zone of internal corrosion with TiN precipitates was observed (see Fig. 5). The decelerating kinetics of this alloy after 7 h is apparently related to MoO_3 and CrO_3 evaporation (see Fig. 3b). The lowest value of the mass gain of the alloy Ta-Mo-Cr-Ti-10Al can be attributed to the formation of porous Ta_2O_5 -rich scales which is accompanied by vaporization of MoO_3 and CrO_3 . The oxidation behaviors of Ta-Mo-Cr-Ti-15Al and Ta-Mo-Cr-Ti-20Al differ significantly from those with the lower Al concentrations. Both alloys exhibit relatively low values of the mass gain (~ 5 mg/cm² after 24 h oxidation at 1200 °C) which can be explained by the formation of continuous $CrTaO_4$ layers. Relevant properties of $CrTaO_4$ manifest themselves in (i) lower oxide scale thickness and (ii) thinner zone of internal corrosion (see Fig. 5e) compared to the alloys that are not able to form a dense $CrTaO_4$ layer. The oxidation kinetics of $CrTaO_4$ -forming superalloys [17] or RHEA [6] seems to approach the oxidation resistance of Cr_2O_3 - and Al_2O_3 -forming Ni-based alloys [22].

CrTaO₄ represents a product of the reaction between Cr₂O₃ and Ta₂O₅. The formation of a continuous CrTaO₄ layer requires certain amounts of both, Cr₂O₃ and Ta₂O₅. The occurrence of Ta₂O₅ in the scales of alloys with 5 and 10 at% Al (Table 1) can be explained by the insufficient amount of Cr₂O₃ formed in the vicinity of Ta₂O₅. In alloys with the higher Al concentrations, all Ta₂O₅ converts to CrTaO₄ (Table 1) because sufficient amount of Cr₂O₃ seems to be available for the reaction between Cr₂O₃ and Ta₂O₅. Our previous investigations revealed that the CrTaO₄ layer slows down oxidation on the equiatomic alloy Ta-Mo-Cr-Ti-Al at 1000 °C and the outer oxide scale consisting of Al₂O₃, Cr₂O₃, TiO₂ particles and a discontinuous Cr₂O₃ scale represents corrosion products which form during transient oxidation [8]. The results generated in the present study confirm that the thickness and the composition of the outer oxide scale formed on the alloy with 20 at% Al after 30 min oxidation at 1200 °C remain almost the same after 24 h of exposure (see Figs. 4d and 5) because the CrTaO₄ layer prevents the outward cation diffusion. Ti forms very stable oxide with extremely high growth rates [18], which explains the largest proportion of Ti besides Al and Cr in the outer layer (Fig. 4). In the present case, the outer oxide layer is mainly composed of TiO₂, while Cr₂O₃ represents a minority phase. A mutual doping, i.e., titanium in chromia and chromium in titania, cannot be excluded. In both cases, however, doping would lead to enhanced growth rates of chromia as well as titania [18, 19]. However, the doping effect would appear during transient oxidation only as the outer scale forms during this stage of oxidation [8] and does not grow during steady-state oxidation (see Fig. 5).

Our recent studies revealed that Ti is present in CrTaO₄ scale formed on the alloy Ta-Mo-Cr-Ti-Al after oxidation at 1000 °C for 48 h [8]. Lo et al. also observed a Ti content of 3.9 at% Ti in the CrTaO₄-based oxide on an RHEA after oxidation at 1100 °C for 200 h [6]. From the theoretical point of view, Ti doping would cause a reduction of oxygen vacancies and therefore a slower growth of the rutile-type CrTaO₄ if Ti⁴⁺ substituted Cr³⁺ cations. In case if Ti⁴⁺ occupies Ta⁵⁺ lattice sites, a contrary effect can be expected. Now, it can, thus, only be speculated whether growth kinetics of CrTaO₄ scales can be slowed down by Ti doping. In-depth theoretical studies supported by experimental investigations are needed to explore the protective potential of CrTaO₄ due to the doping effect. Figure 6 proves that the amount of Cr and therefore Cr₂O₃ in the outer scale enhances with the Al content obviously leading to the formation of a dense CrTaO₄ layer in alloys with 15 and 20 at. % Al. Furthermore, Fig. 5 reveals that the penetration depth of internal Al₂O₃ increases with increasing Al content.

The positive effect of Al on the formation of Cr₂O₃ can be attributed to the (i) getter effect and (ii) nucleation effect as well as (iii) enhanced Cr diffusion in the Al-depleted zone. Due to its higher affinity to oxygen, Al acts as a getter as it oxidizes externally and internally allowing Cr to diffuse to the surface to participate in the formation of CrTaO₄. This effect was proposed by Wood et al. to explain the oxidation behavior of Co-Cr-Al alloys [20]. Giggins et al. [21] also reasoned the facilitated formation of a continuous Cr₂O₃ oxide layer in Ni-Cr-Al alloys by the getter effect of Al. It should, however, be mentioned that the aforementioned getter effect may only be significant a relatively short period of oxidation as Al oxidizes internally very fast due to the high thermodynamic stability of its oxide (see Fig. 5).

Further, it is well-known that Al_2O_3 serves as a nucleation site for Cr_2O_3 [20]. This effect can also be assumed operative in case of the RHEA investigated here. The beneficial effect of Al on the nucleation and growth of Cr_2O_3 in Co-Cr-Al [20] was concluded by Woods et al. This statement was supported by Yun et al. who reported that Al can act as nucleation site for Cr_2O_3 like a reactive element in Ni-Cr-Wo-Mo-Al alloys [22]. Finally, internally oxidized Al may have a positive effect on the formation of chromia in the near-surface regions. Chyrkin et al. demonstrated that Cr activity enhances with an increasing Al content in Ni-Cr-Al alloys [23]. In the region with internal alumina precipitates, both Al and Cr activities are reduced. This results in a Cr gradient in the alloy and, thus, in an additional driving force for Cr diffusion toward the surface and an increased Cr flux, which supports the chromia formation in the near-surface region. In case of our alloy, the thick zones of internal corrosion in alloys with higher Al concentrations may facilitate enhanced Cr diffusion to the surface in order to compensate the reduction in the Cr activity due to internal oxidation of Al.

Summary

In this paper, the effect of Al on the high temperature oxidation resistance of the RHEA Ta-Mo-Cr-Ti-xAl ($x=5; 10; 15; 20$ at%) was studied. Experimental results clearly reveal that Al substantially improves the oxidation resistance of these alloys. The oxidation kinetics is severely influenced by the evaporation of MoO_3 and CrO_3 . The thicknesses of the oxide scales and the zone of internal corrosion decrease successively with the increasing Al content. While the alloys with 5 and 10 at% Al form thick oxide layers because of the formation of fast growing Ta_2O_5 , the alloys with 15 and 20 at% Al exhibit relatively thin oxide scales due to the formation of a continuous CrTaO_4 layer at the interface oxide/substrate. It is suggested that Al supports the formation of Cr_2O_3 and, finally, CrTaO_4 because of the getter effect of Al which preferentially consumes oxygen enabling Cr to diffuse to the surface to participate in the formation of a relatively protective CrTaO_4 layer. It is also suggested that Al promotes the nucleation of Cr_2O_3 further facilitating the growth of CrTaO_4 to a compact scale.

Acknowledgements The financial support by Deutsche Forschungsgemeinschaft (DFG), Grant No. HE 1872/34-2 is gratefully acknowledged. Part of this work was performed at the Micro- and Nanoanalytics Facility (MNAF) of the University of Siegen.

Funding Open Access funding enabled and organized by Projekt DEAL.


Open Access This article is licensed under a Creative Commons Attribution 4.0 International License, which permits use, sharing, adaptation, distribution and reproduction in any medium or format, as long as you give appropriate credit to the original author(s) and the source, provide a link to the Creative Commons licence, and indicate if changes were made. The images or other third party material in this article are included in the article's Creative Commons licence, unless indicated otherwise in a credit line to the material. If material is not included in the article's Creative Commons licence and your intended use is not permitted by statutory regulation or exceeds the permitted use, you will need to obtain permission directly from the copyright holder. To view a copy of this licence, visit <http://creativecommons.org/licenses/by/4.0/>.

References

1. J.-W. Yeh, S.-K. Chen, S.-J. Lin, J.-Y. Gan, T.-S. Chin, T.-T. Shun, C.-H. Tsau, S.-Y. Chang, *Advanced Engineering Materials*. **6**, 299 (2004).
2. O.N. Senkov, G.B. Wilks, D.B. Miracle, C.P. Chuang, P.K. Liaw, *Intermetallics*. **18**, 1758 (2010).
3. O.N. Senkov, G.B. Wilks, J.M. Scott, D.B. Miracle, *Intermetallics*. **19**, 698 (2011).
4. H. Chen, A. Kauffmann, S. Seils, T. Boll, C.H. Liebscher, I. Harding, K.S. Kumar, D.V. Szabó, S. Schlabach, S. Kauffmann-Weiss, F. Müller, B. Gorr, H.-J. Christ, M. Heilmaier, *Acta Materialia*. **176**, 123 (2019).
5. O.N. Senkov, D.B. Miracle, K.J. Chaput, J.-P. Couzinie, *Journal of Materials Research*. **33**, 3092 (2018).
6. K.-C. Lo, Y.-J. Chang, H. Murakami, J.-W. Yeh, A.-C. Yeh, *Scientific reports*. **9**, 7266 (2019).
7. K.-C. Lo, H. Murakami, J.-W. Yeh, A.-C. Yeh, *Intermetallics*. **119**, 106711 (2020).
8. F. Müller, B. Gorr, H.-J. Christ, J. Müller, B. Butz, H. Chen, A. Kauffmann, M. Heilmaier, *Corrosion Science*. **159**, 108161 (2019).
9. E.P. George, W.A. Curtin, C.C. Tasan, High entropy alloys, *Acta Materialia*. **188**, 435 (2020).
10. L.-C. Li, M.-X. Li, M. Liu, B.-Y. Sun, C. Wang, J.-T. Huo, W.-H. Wang, Y.-H. Liu, *Science China Materials*. DOI <https://doi.org/10.1007/s40843-020-1332-2> (2020).
11. P. Massard, J.C. Bernier, A. Michel, *Journal of Solid State Chemistry*. **4**, 269 (1972).
12. F. Schlottig, J. Schreckenbach, G. Marx, *Journal of Analytical Chemistry*. **363**, 209 (1999).
13. B. Gorr, F. Müller, S. Schellert, H.-J. Christ, H. Chen, A. Kauffmann, M. Heilmaier, *Corrosion Science*. **166**, 108475 (2020).
14. F. Müller, B. Gorr, H.-J. Christ, H. Chen, A. Kauffmann, S. Laube, M. Heilmaier, *Journal of Alloys and Compounds*. **842**, 155726 (2020).
15. J. P. Kofstad, *Journal of the Less Common Metals*. **7**, 241 (1964).
16. T.E. Tietz, J.W. Wilson, *Behavior and properties of refractory metals*. Stanford Univ. Pr, Stanford, Calif., (1965).
17. W. Ren, F. Ouyang, B. Ding, Y. Zhong, J. Yu, Z. Ren, L. Zhou, *Journal of Alloys and Compounds*. **724**, 565 (2017).
18. J. P. Kofstad, *High Temperature Oxidation of Metals*, New York: John Wiley & Sons, 1966, 169-178.
19. A. Jalowicka, W. Nowak, D. Naumenko, L. Singheiser, W. J. Quadackers, *Materials and Corrosion*. **65**, 178 (2014).
20. G. C. Wood, F. H. Stott, *Oxidation of Metals*. **3**, 365 (1971).
21. C. S. Giggins, F. S. Pettit, *Journal of The Electrochemical Society*. **118**, 11 (1971).
22. D.W. Yun, S.M. Seo, H.W. Jeong, Y.S. Yoo, *Corrosion Science*. **83**, 176 (2014).
23. A. Chyrkin, W. G. Sloof, R. Pillai, D. Grüner, L. Singheiser, W. J. Quadackers, *Materials at High Temperatures*. **32**, 102 (2015)

Publisher's Note Springer Nature remains neutral with regard to jurisdictional claims in published maps and institutional affiliations.

Authors and Affiliations

S. Schellert¹  · **B. Gorr**² · **H.- J. Christ**¹ · **C. Pritzel**³ · **S. Laube**² · **A. Kauffmann**² · **M. Heilmaier**²

B. Gorr
bronislava.gorr@kit.edu

H.- J. Christ
hans-juergen.christ@uni-siegen.de

C. Pritzel
pritzel@chemie.uni-siegen.de

S. Laube
stephan.laube@kit.edu

A. Kauffmann
alexander.kauffmann@kit.edu

M. Heilmaier
martin.heilmaier@kit.edu

¹ Institut Für Werkstofftechnik, Universität Siegen, Siegen, Germany

² Institut Für Angewandte Materialien, Karlsruher Institut Für Technologie (KIT), Karlsruhe, Germany

³ Institut Für Bau- Und Werkstoffchemie, Universität Siegen, Siegen, Germany